Flight path reconstruction filter extension for tracking flexible aircraft modal amplitudes and velocities

Jurisson, A.; Eussen, Bart; de Visser, C.C.; De Breuker, R.

DOI
10.2514/6.2023-0626

Publication date
2023

Document Version
Final published version

Published in
AIAA SciTech Forum 2023

AIAA SciTech Forum
23-27 January 2023, National Harbor, MD & Online
AIAA SCITECH 2023 Forum

10.2514/6.2023-0626

Flight path reconstruction filter extension for tracking flexible aircraft modal amplitudes and velocities

A. Jürisson* and B. Eussen†
Netherlands Aerospace Centre, 1059 CM, Amsterdam, The Netherlands

C.C. de Visser ‡ and R. de Breuker.§
Delft University of Technology, 2629 HS, Delft, The Netherlands

This paper proposes an extension to the traditional flight path reconstruction filter to simultaneously reconstruct the aircraft rigid body states together with modal amplitudes and velocities of the structure. To achieve this, the filter makes use of additional accelerometers, gyroscopes and strain gauges placed across the aircraft structure. These measurements are used in a Kalman filter together with kinematic equations of a flexible aircraft and structural mode shapes. First a simulation model is used to evaluate the filter performance on reference signals where the true state is known. Finally, flight test measurements obtained using an instrumented Diana 2 scaled glider are used to validate the filter.

I. Introduction

Flight testing is a core part of the development process of any new aircraft. As part of the testing, the aircraft responses during various manoeuvres are recorded from which aircraft stability coefficients describing its characteristics can be determined. These estimates can then be used to validate or update existing numerical models. However, the measured responses are noisy, biased and possibly sampled at different rates which can lead to inaccuracies in the models. For this reason, flight path reconstruction (FPR) [1, 2] is often the first step in filtering and checking consistency of gathered flight test data before estimating these stability coefficients. FPR is a filtering technique where the time history of the aircraft's state is reconstructed by combining aircraft kinematic equations with the response measurements. In these equations, the aircraft is represented as a point mass moving through the air. However, in order to become more fuel efficient the aircraft structures are becoming lighter and thereby also more flexible. This in turn results in the structural dynamics of the aircraft having a larger interaction with the aircraft flight dynamic response. Therefore, in order to model this interaction correctly, it is necessary to also reconstruct the dynamics of the structure together with the rigid body states.

In addition to aeroelastic modelling, tracking the aircraft structural deformation is also important for applications such as structural health monitoring and active control for load and gust alleviation, drag reduction or flutter suppression [3]. For this reason, in literature many approaches have been explored to track the aircraft wing deflections, shape or the state of the whole structure. Solutions based on different sensors and sensor combinations have been proposed. One approach is to use only strain measurements either from strain gauges or fiber bragg grating sensors. These can be either directly integrated into a displacement estimate, converted into modal amplitudes using strain modes or combined with a Finite Element Method (FEM) model to obtain a fit of the wing shape [4–6]. These strain sensors need to be integrated to the structure and many measurement points and/or an accurate FEM model are required to achieve good tracking [3]. A nonintrusive alternative is to use camera based solutions that estimate deformations by tracking markers placed on the wings [7–9]. However, when using only cameras, the tracking accuracy can be greatly influenced by lighting and visibility conditions and obtaining high sampling rates is challenging. For this reason, recent studies have also explored using a combination of different sensors such as accelerometers+cameras [10], gyroscopes+cameras [11], accelerometers+gyroscopes [12] or accelerometers+strain gauges [3] to reconstruct the structural deformations.

However, for aeroelastic modelling it is desirable to simultaneously reconstruct the structural dynamics and also the states related to the aircraft rigid body motion. In this paper, an extension to the traditional FPR filter is created

*Ph.D. Candidate, Flight Physics and Loads Department, Andres.Jurisson@nlr.nl, 1059 CM, Amsterdam, The Netherlands.
†Senior Researcher, Flight Physics and Loads Department, Bart.Eussen@nlr.nl, 1059 CM, Amsterdam, The Netherlands.
‡Associate Professor, Faculty of Aerospace Engineering, Control and Simulation Division, c.c.devisser@tudelft.nl, 2629 HS Delft, The Netherlands
§Associate Professor, Faculty of Aerospace Engineering, Aerospace Structures and Computational Mechanics Division, R.DeBreuker@tudelft.nl, 2629 HS Delft, The Netherlands.

that allows to estimate the aircraft rigid body states together with modal amplitudes and velocities of the structure. To achieve this, the proposed method makes use of additional accelerometer, gyroscope and strain gauge measurements collected from across the aircraft. It is not required to have a flight dynamics model of the aircraft. Instead the mode shapes of interest with respect to the sensor locations need to be provided.

The paper is organized as follows. In Sec. II the FPR filter equations are extended to incorporate the tracking of modal amplitude and velocity by the means of additional sensors. Then in Sec. III the scaled glider model is presented that is used as a reference model for the simulation study and flight testing. A simulation study of the filter performance is presented in Sec. IV followed by flight testing results in Sec. V. Finally Sec. VI summarises the main findings of the paper.

II. Theoretical background

The proposed filter uses an Extended Kalman filter together with a model derived from the mean-axis formulation [13, 14] and is an extension of the traditional flight path reconstruction filters. This approach makes use of additional accelerometers, gyroscopes and strain gauges distributed along the flexible aircraft structure, to be able to reconstruct the aircraft flight path together with the modal amplitudes and modal velocities.

In the center of a Kalman filter is a model of the system's dynamics that describes the evolution of that system and is used to predict and correct the system responses. For a nonlinear system and Kalman filter the system is represented in the following format:

$$\dot{X} = f(X, U) + w \tag{1}$$

$$Y = h(X) + v \tag{2}$$

Here X is a vector for system states, U represents the system inputs, Y system outputs and w and v are for process and measurement noise respectively. The evolution of the system state is represented by nonlinear function f and output is determined by nonlinear function h.

In the case of the extension to the flight path reconstruction filter presented in this paper, these equations represent the kinematics of a flexible aircraft. Therefore, the states that are being estimated using the filter are as follows:

$$X = [x\ y\ z\ u\ v\ w\ \phi\ \theta\ \psi\ p\ q\ r\ \dot{\eta}\ \eta\ \lambda]^T \tag{3}$$

The variables $x,\ y,\ z$ represent the aircraft position in the Earth fixed reference frame, $u,\ v,\ w$ are the velocity components in the Body reference frame and $\phi,\ \theta,\ \psi$ are the roll, pitch and yaw angles, $p,\ q,\ r$ are the aircraft center of gravity rotational rates, $\dot{\eta},\ \eta$ are vectors containing the modal velocities and amplitudes. Finally, λ is a vector containing all the unknown biases that are estimated as part of the filtering process:

$$\lambda = [\lambda_{A_x}\ \lambda_{A_y}\ \lambda_{A_z}\ \lambda_p\ \lambda_q\ \lambda_r\ \lambda_\alpha\ \lambda_\beta\ ] \tag{4}$$

Here $\lambda_{A_x}\ \lambda_{A_y}\ \lambda_{A_z}$ are the center of gravity accelerometer sensor biases, $\lambda_p,\ \lambda_q,\ \lambda_r$ are the biases for the center of gravity gyroscope and $\lambda_\alpha,\ \lambda_\beta$ are biases for aerodynamic angle measurements.

Traditionally, wind is also added to the filter as a constant bias term or a Markov process [1]. However, this was not suitable as the flight testing was conducted at low altitude with rapidly changing wind speed and direction. Fortunately, it was possible to estimate the wind speed by determining the difference between the aircraft velocity measured in the Earth frame by the GPS and the airspeed measured by the aeroprobe which was converted to Earth frame using aerodynamic angle and attitude measurements.

$$W^E = T_{Eb}\ T_{ba}\ V^a_{probe} - V^E_{GPS} \tag{5}$$

Where W^E is a wind speed vector in Earth frame, V^a_{probe} is the airspeed by the aeroprobe and V^E_{GPS} is the aircraft velocity given by the GPS while the transformation matrix from body-fixed frame to Earth frame is given by Eq. 6 and from aerodynamic frame to aircraft body-fixed is given by Eq. 7.

$$T_{Eb}(\phi, \theta, \psi) = \begin{bmatrix} \cos\theta\cos\psi & \sin\phi\sin\theta\cos\psi - \cos\phi\sin\psi & \cos\phi\sin\theta\cos\psi + \sin\phi\sin\psi \\ \cos\theta\sin\psi & \sin\phi\sin\theta\sin\psi + \cos\phi\cos\psi & \cos\phi\sin\theta\sin\psi - \sin\phi\cos\psi \\ -\sin\theta & \sin\phi\cos\theta & \cos\phi\cos\theta \end{bmatrix} \tag{6}$$

$$T_{ba}(\alpha,\beta) = \begin{bmatrix} \cos\beta\cos\alpha & -\sin\beta\cos\alpha & -\sin\alpha \\ \sin\beta & \cos\beta & 0 \\ \cos\beta\sin\alpha & -\sin\beta\sin\alpha & \cos\alpha \end{bmatrix} \tag{7}$$

This allowed to provide the wind speed as an input to the filter together with all the accelerations A_N and rotational accelerations $\dot{\omega_N}$ measured by in total N sensors placed across the aircraft structure. The rotational accelerations were obtained through numerical differentiation of the gyroscope measurements. The complete input vector is then as follows:

$$U = [W^E \; A_N \; \dot{\omega}_N]^T \tag{8}$$

Next, the system state equations are determined. In a flexible aircraft, the accelerations measured across the structure include the acceleration of the aircraft center of gravity but also effects due to the structural dynamics and effects due to the aircraft rotation. The acceleration measured by sensor k on the flexible aircraft can be found using Eq. 9 [14].

$$A_k = A_{cg} + \dot{\omega}_{cg} \times (r + \Phi_k\eta) + \omega_{cg} \times [\omega_{cg} \times (r + \Phi_k\eta)] + \Phi_k\ddot{\eta} + (2\omega_{cg} \times \Phi_k\dot{\eta}) \tag{9}$$

Here A_{cg} and ω_{cg} correspond to the acceleration and rotational rate of the aircraft center of gravity. The modal acceleration vector is $\ddot{\eta}$ while Φ_k is the mode shape corresponding to the sensor location and r is the sensor distance to aircraft center of gravity. Similarly, the rotational accelerations measured across the aircraft structure are also influenced by the structural dynamics. The rotational acceleration measured by sensor k can be found using Eq. 10.

$$\dot{\omega}_k = \dot{\omega}_{cg} + H_k\ddot{\eta} \tag{10}$$

Here H_k is the rotational shape corresponding to the sensor location. Combining and rearranging these two equations it is possible to arrive at the following matrix multiplication:

$$\begin{bmatrix} A_k - \omega_{cg} \times [\omega_{cg} \times (r_k + \Phi_k\eta)] - (2\omega_{cg} \times \Phi_k\dot{\eta}) \\ \dot{\omega}_k \end{bmatrix} = \underbrace{\begin{bmatrix} I & R & \Phi_k \\ 0 & I & H_k \end{bmatrix}}_{G_k} \begin{bmatrix} A_{cg} \\ \dot{\omega}_{cg} \\ \ddot{\eta} \end{bmatrix} \tag{11}$$

Here R is the skew-symmetric matrix to represent the $\dot{\omega}_{cg} \times (r + \Phi_k\eta)$ cross product as a matrix multiplication and I is the identity matrix. When the amplitude of the deformations is small, the $\Phi_k\eta$ and $\Phi_k\dot{\eta}$ terms can be assumed to be zero. By repeating this process for all N sensors, it is possible to estimate the aircraft center of gravity translation, rotation and modal accelerations through a least squares fit of the combined mode shape matrix.

$$\begin{bmatrix} A_{cg} \\ \dot{\omega}_{cg} \\ \ddot{\eta} \end{bmatrix} = \begin{bmatrix} G_1 \\ \vdots \\ G_N \end{bmatrix}^{\dagger} \begin{bmatrix} A_1 - \omega_{cg} \times [\omega_{cg} \times (r_1 + \Phi_1\eta)] - (2\omega_{cg} \times \Phi_1\dot{\eta}) \\ \dot{\omega}_1 \\ \vdots \\ A_N - \omega_{cg} \times [\omega_{cg} \times (r_N + \Phi_N\eta)] - (2\omega_{cg} \times \Phi_N\dot{\eta}) \\ \dot{\omega}_N \end{bmatrix} \tag{12}$$

It is important to choose the amount and location of the sensors such that they provide sufficient information about the modes selected for reconstruction. The sensor placement can be evaluated by determining the condition number of the combined mode shape matrix, where a value closer to 1 is desirable:

$$\kappa(\Phi) = \|\Phi\| \left\|\Phi^{\dagger}\right\| \tag{13}$$

With the estimates for the center of gravity and modal accelerations, it is now possible to combine them with the rigid aircraft kinematic equations to extend the flight path reconstruction filter for a flexible aircraft case. The time derivatives for the filter states presented in Eq. 3 are as follows with $A_{cg}, \dot{\omega}_{cg}, \ddot{\eta}$ found using Eq. 12:

$$\begin{bmatrix}\dot{x}\\ \dot{y}\\ \dot{z}\end{bmatrix} = T_{Eb}\begin{bmatrix}u\\ v\\ w\end{bmatrix} + W^E \tag{14}$$

$$\begin{bmatrix}\dot{u}\\ \dot{v}\\ \dot{w}\end{bmatrix} = A_{cg} + \begin{bmatrix}0 & -w & v\\ w & 0 & -u\\ -v & u & 0\end{bmatrix}\begin{bmatrix}p\\ q\\ r\end{bmatrix} + T_{bE}\begin{bmatrix}0\\ 0\\ g\end{bmatrix} \tag{15}$$

$$\begin{bmatrix}\dot{\phi}\\ \dot{\theta}\\ \dot{\psi}\end{bmatrix} = \begin{bmatrix}1 & \sin\phi\tan\theta & \cos\phi\tan\theta\\ 0 & \cos\phi & -\sin\phi\\ 0 & \frac{\sin\phi}{\cos\theta} & \frac{\cos\phi}{\cos\theta}\end{bmatrix}\begin{bmatrix}p\\ q\\ r\end{bmatrix} \tag{16}$$

$$\begin{bmatrix}\dot{p}\\ \dot{q}\\ \dot{r}\end{bmatrix} = \dot{\omega}_{cg} \tag{17}$$

$$\begin{bmatrix}\ddot{\eta}\\ \dot{\eta}\end{bmatrix} = \begin{bmatrix}\ddot{\eta}\\ \dot{\eta}\end{bmatrix} \tag{18}$$

$$\begin{bmatrix}\dot{\lambda}\end{bmatrix} = 0 \tag{19}$$

Next, the filter output equations are determined. Again, first the standard FPR output equations are presented with aircraft position, attitude, velocity, aerodynamic angle measurements and GPS velocities [1] where v_* represents white noise on the measurement.

$$Y = \begin{bmatrix}x\\ y\\ z\\ \phi\\ \theta\\ \psi\\ V_{probe}\\ \alpha\\ \beta\\ V_{GPS_x}\\ V_{GPS_y}\\ V_{GPS_z}\end{bmatrix}_m = \begin{bmatrix}x\\ y\\ z\\ \phi\\ \theta\\ \psi\\ \sqrt{u^2+v^2+w^2}\\ \tan^{-1}(\frac{w}{u}) + \lambda_\alpha\\ \tan^{-1}(\frac{v}{u}) + \lambda_\beta\\ T_{Eb}\begin{bmatrix}u\\ v\\ w\end{bmatrix} + W^E\end{bmatrix} + \begin{bmatrix}v_x\\ v_y\\ v_z\\ v_\phi\\ v_\theta\\ v_\psi\\ v_V\\ v_\alpha\\ v_\beta\\ v_{Vx}\\ v_{Vy}\\ v_{Vz}\end{bmatrix} \tag{20}$$

For the flexible aircraft, additional output equations are required to be able to also correct the modal velocity and amplitude estimates. Strain gauge measurements collected across the aircraft structure can be used to aid in tracking the modal amplitudes. The measured strains can be approximated as a summation of strain modes scaled by the modal amplitudes as shown in Eq.21.

$$\epsilon_k = \Psi_k\eta + v_\epsilon \tag{21}$$

Here ϵ_k is the measured strain and Ψ_k is the strain mode shape matrix corresponding to that sensor and v_ϵ is noise. Furthermore, the rotational rates collected across the flexible aircraft structure using gyroscopes are also added. The measured rotational rates include the rotational rate of the aircraft rigid body and the effects due to structural dynamics as shown in Eq. 22.

$$\omega_k = \omega_{cg} + H_k\dot{\eta} + v_\omega \tag{22}$$

Here ω_k is the measured rotational rate and H_k is the rotational mode shape matrix corresponding to that sensor.

III. Reference model

A 1 to 3 scaled Diana 2 glider is used as a test aircraft to validate the working principle of the filter with flight data. A numerical model of this glider is also built for a simulation study. For flight testing the glider is instrumented with numerous sensors placed across the entire aircraft. These included inertial measurement units (IMUs), strain gauges, GPS sensor, a 5-hole aeroprobe and other sensors as presented in [15]. An overview of the sensors used by the filter and their locations are presented in Fig. 1. At each IMU location the accelerations and rotational rates on all 3-axis are measured while both shear and bending strains are measured at each strain gauge location. In total 36 accelerations and rotational rates and 21 strains are measured. All measurements were resampled to 250Hz and a low-pass filter with 60Hz cutoff was applied before using the Kalman filter.

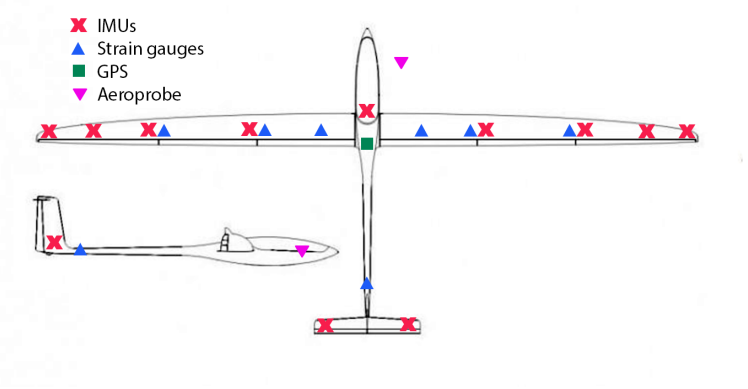

Fig. 1 Diana 2 sensor placement overview.

The main technical parameters of the scaled glider are presented in Table 1 while an image of the glider is presented in Fig. 2.

Table 1 Diana 2 model technical data.

Property	Symbol	Value
Aspect ratio	Λ	24.3
Wingspan	b	5.0 m
Wing area	S	1.03 m^2
Mean chord	$\bar{c}$	0.206 m
Weight	m	11.25 kg

Fig. 2 Diana 2 1:3 scaled glider [15].

To be able to simulate and generate response measurements for an aeroelastic aircraft, a flight dynamics simulation model was also created. This allows to evaluate the performance of the filter as the true states of the system are known. First, a Finite Element Method (FEM) model of this scaled glider was created and updated using ground vibration test measurements as presented in [16]. Using the FEM model together with aerodynamic panels created based on an outline scan of the glider, it was possible to create an aeroservoelastic model of the aircraft using ZAERO software. This model was then implemented in Simulink to be able to fly reference manoeuvres in real time.

The implemented flight dynamics model is based on the mean axis formulation [13, 14]. An overview of the equations that govern the movement of the aircraft centre of gravity together with the structural dynamics are presented in Eq. 23 to 29.

$$\bar{q}SC_x = m\dot{u} + m(qw - rv) + mg\sin\theta \tag{23}$$

$$\bar{q}SC_y = m\dot{v} + m(ru - pw) - mg\cos\theta\sin\phi \tag{24}$$

$$\bar{q}SC_z = m\dot{w} + m(pv - qu) - mg\cos\theta\cos\phi \tag{25}$$

$$\frac{\bar{q}Sb}{Ix}C_l = \dot{p} - \frac{I_{xz}}{I_x}\dot{r} + \frac{I_z - I_y}{I_x}qr - \frac{I_{xz}}{I_x}qp \tag{26}$$

$$\frac{\bar{q}S\bar{c}}{I_y}C_m = \dot{q} - \frac{I_x - I_z}{I_y}pr + \frac{I_{xz}}{I_y}(p^2 - r^2) \tag{27}$$

$$\frac{\bar{q}Sb}{I_z}C_n = \dot{r} - \frac{I_{xz}}{I_z}\dot{p} + \frac{I_y - I_x}{I_z}pq + \frac{I_{xz}}{I_z}qr \tag{28}$$

$$\frac{\bar{q}S\bar{c}}{m_i}C_{Q_i} = \ddot{\eta}_i + 2\xi_i\omega_i\dot{\eta}_i + \omega_i^2\eta_i \tag{29}$$

The aerodynamic forces coefficients C_x, C_y, C_z and moment coefficients C_l, C_m, C_n are obtained from ZAERO together with the generalized force coefficient C_{Q_i}. The state η_i represents the i-th modal amplitude and m_i is the corresponding generalised mass. The corresponding natural frequency ω_i and damping ξ_i were determined during the ground vibration testing. The dynamic pressure $\bar{q}$ corresponds to the simulation airspeed and wing area S and moment of inertia I_* are properties of the aircraft.

The first 14 structural modes were included in the aeroelastic model which covers a frequency range up to 60Hz. In addition to the traditional displacement mode shapes also the rotational and strain modes needed to be determined during the vibration testing as they are required by the filter. In Fig. 3 to Fig. 6 the first four structural modes are presented as an example outcome of such a test. In these figures, the displacement corresponds to displacement mode shapes, arrows correspond to rotational mode shapes and blue/red colours show compression and tension of the strain shapes.

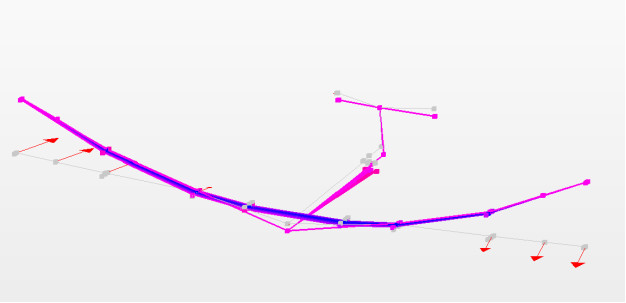

Fig. 3 Mode 1 - 1st sym. wing bending.

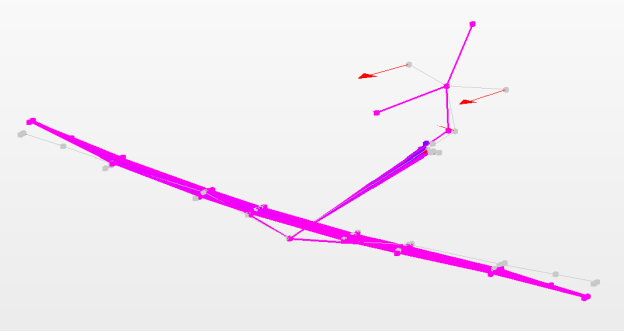

Fig. 4 Mode 2 - tail rotation around x-axis.

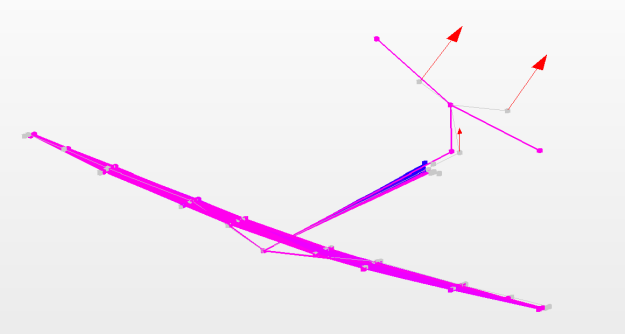

Fig. 5 Mode 3 - tail rotation around z-axis.

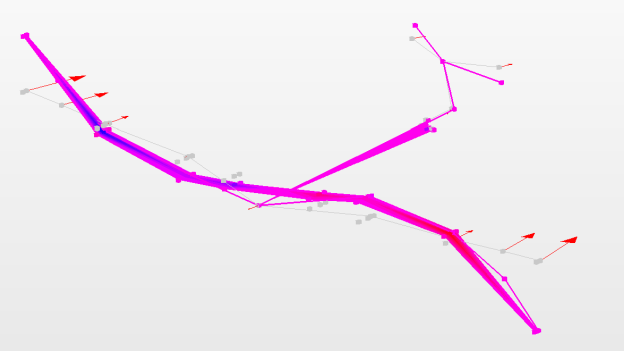

Fig. 6 Mode 4 - 2nd asym. wing bending.

IV. Simulation study

A. Reference signal generation

With the flight dynamics simulator of the flexible aircraft implemented, it was possible to generate reference responses for the filter. Sine sweeps on the ailerons, elevator and rudder were chosen for the control surface inputs as they are able to excite both the aircraft rigid body dynamics and a range of structural modes. In order to evaluate the performance of the filter, noise was added to the simulated response signals before applying the filter. Overview of the used noise standard deviations are presented in Table 2. The chosen values are similar or even more conservative than the sensor values used during the flight tests.

Table 2 Noise standard deviations.

Signal	Noise	Units
Acceleration	0.05	m/s^2
AoA, AoS	0.2	deg
Attitude	1.5	deg
Rotational rates	0.3	deg/s
Strain	1.0	microstrain
V_{GPS}	1.0	m/s
V_{probe}	0.5	m/s
Position XY	1.3	m
Position Z	0.3	m
Wind	2.0	m/s

B. Filter performance

After adding noise to the simulation responses, the filter was applied. First the states and measurements related to the rigid body motion were assessed. In Fig. 7 the aircraft attitude tracking together with aerodynamic angles are presented for an elevator sine sweep. As can be seen, the filter is able to accurately reconstruct the aircraft rigid body signals from the noisy measurements with less than 0.1 deg root mean squared error for the attitude and aerodynamic angles.

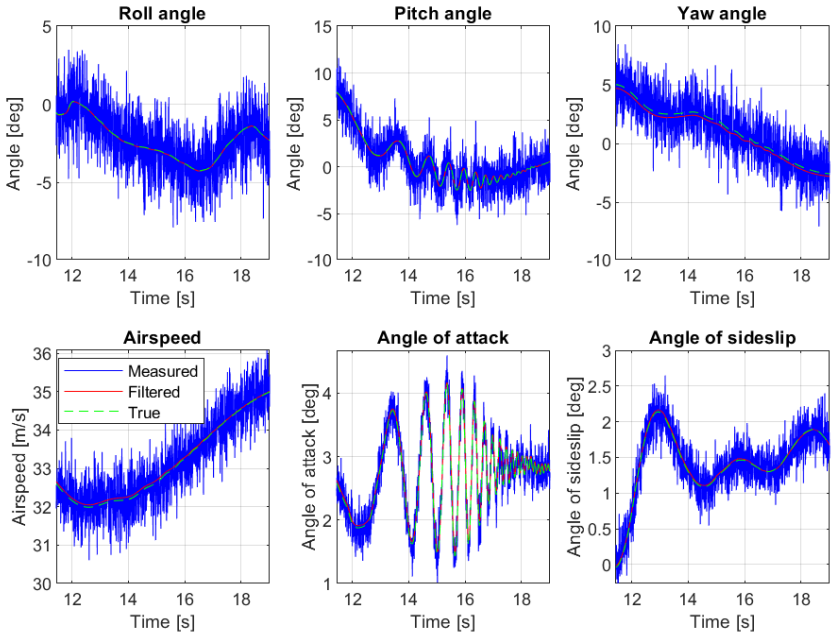

Fig. 7 Aircraft attitude and aerodynamic angle signal tracking, simulation study.

Next, the modal tracking is explored. In addition to tuning the noise parameters for each signal, it is now also necessary to provide the mode shapes of modes that wish to be reconstructed. In order to evaluate the tracking performance sensitivity to the amount of modes used in the filter, the reconstruction was performed while adding higher order modes one by one. In Fig. 8 and Fig. 9 the amplitude and velocity tracking for mode 1 and mode 3 are presented for varying number of total modes N included in the filter.

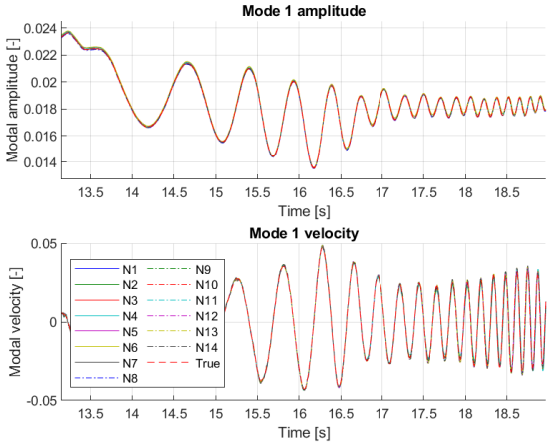

Fig. 8 Mode 1 amplitude and velocity tracking for varying number of modes in the filter.

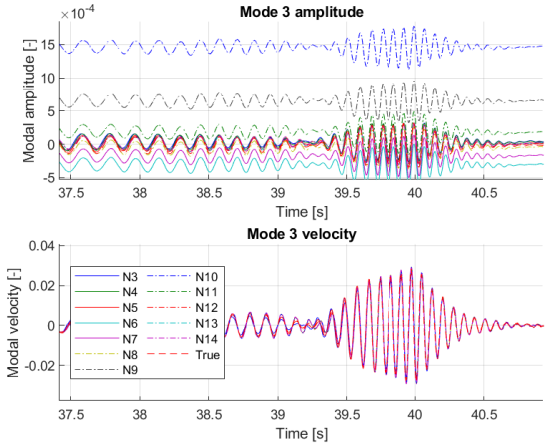

Fig. 9 Mode 3 amplitude and velocity tracking for varying number of modes in the filter.

As can be seen, both modal amplitude and velocity have been accurately reconstructed and the tracking results remain consistent when higher order modes are added to the filter. However, in some cases an offset in the modal amplitude responses can be observed as shown in Fig. 9. As more modes get added, a better fit of the responses can be achieved by readjusting the existing mode amplitudes. Therefore, different constant offsets for the modal amplitudes can be observed but the dynamics of the mode is still well captured. This can be seen in Fig. 10 where the relative root mean square (RMS) error is found for each mode as shown in Eq. 30. The $\hat{\eta}$ represents here the true modal amplitude and η is the filtered. This was repeated also for the modal velocities.

$$RMS_{rel} = \frac{\sqrt{\frac{1}{N}\sum_{i=1}^{N}(\hat{\eta}_i - \eta_i)^2}}{|max(\hat{\eta}) - min(\hat{\eta}))|} \tag{30}$$

In this case, the constant offset in the modal amplitudes was removed beforehand to compare the reconstructed signal dynamics. The tracking errors for each mode remain close to constant values as additional modes are added. Only for mode 7 a large drop in the modal amplitude error was seen after adding mode 8. This is due to both of the modes being second symmetric bending modes very similar in shape. This requires both of them to be present in the filter to correctly reconstruct their contributions. While adding more modes leads to a better overall fit, there is a limit where the higher order modes can no longer be correctly distinguished from the sensor noise. This can be seen for modes 9, 11 and 14 which show large errors for modal amplitude reconstruction. Nevertheless, the addition of these modes to the filter does not degrade the reconstruction of the other lower order modes.

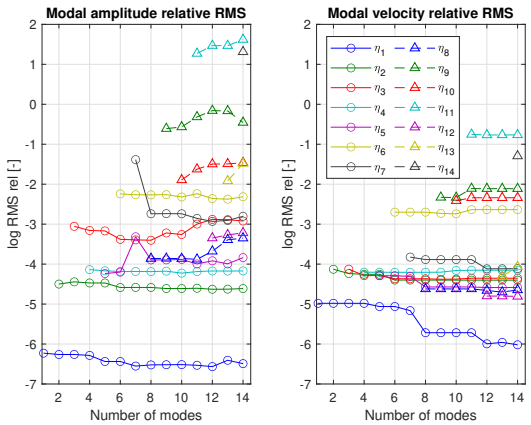

Fig. 10 Modal amplitude and velocity tracking relative RMS error for varying modes included to the filter.

Until now, the mode shapes in the simulation model used to create the reference responses and the filter have been identical. However, in the real world this is very unlikely. Therefore, to check the filter sensitivity for mismatches and errors in the mode shapes all the mode shape entries were randomly varied by up to ±15%. This was implemented by multiplying the values with a random gain matrix with a 5% standard deviation. In total 250 separate runs with random mode shape variations were performed. In Fig. 11 and Fig. 12 again the modal amplitude and velocity reconstruction for modes 1 and 3 are shown. Here the true modal response is shown together with the mean response across all the runs and the area covering two standard deviations of the variations in the responses. As can be seen, even with the perturbations applied on the mode shapes the filter is able to closely reconstruct the modal responses.

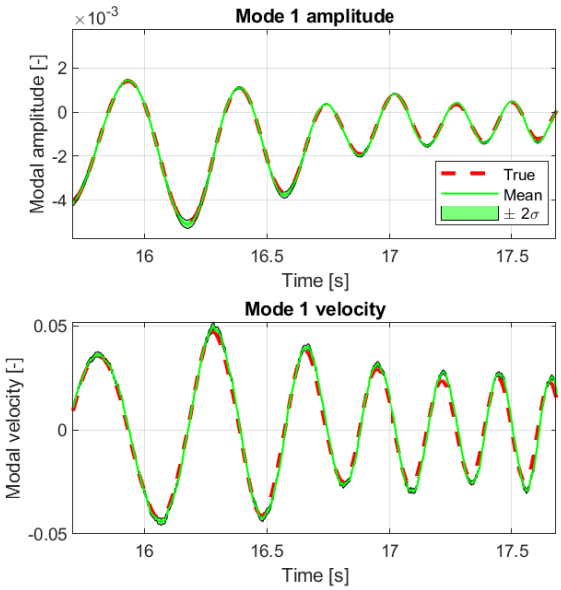

Fig. 11 Mode 1 amplitude and velocity tracking with mode shape perturbations.

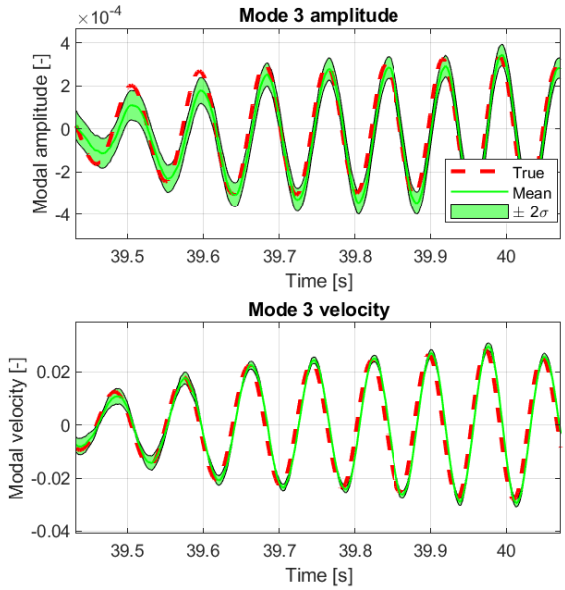

Fig. 12 Mode 3 amplitude and velocity tracking with mode shape perturbations.

V. Flight testing results

After evaluating the filter performance using simulated responses, it was now possible to apply it on measurements collected during flight testing. From the flight tests a section that covers manually executed sine sweeps on the elevator was selected for evaluation as it is most comparable to the simulation study. Again, first the states related to the rigid body motion were evaluated. In Fig. 13 the aircraft attitude and aerodynamic angle tracking are presented. With flight data we do not know the true signal values which is the reason for using the filter in the first place. However, we can compare the results with the traditional FPR filter output that is using the same noise parameters.

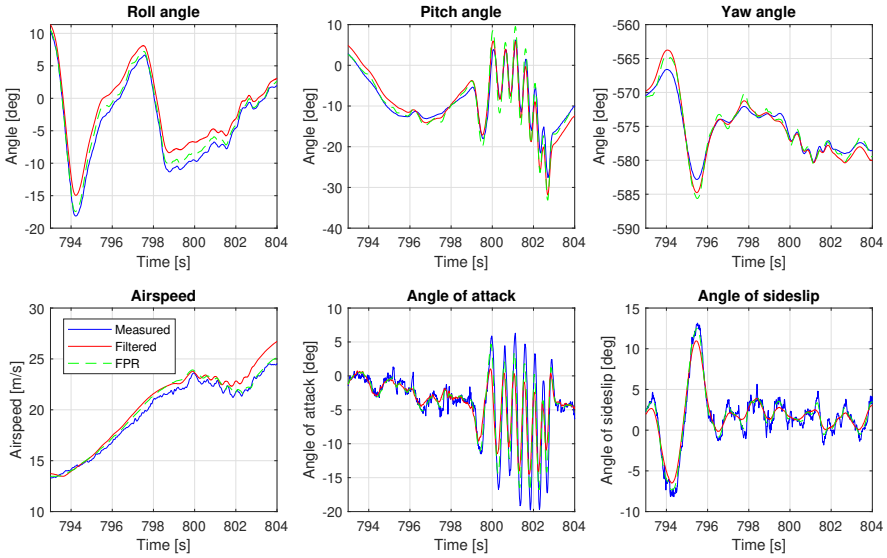

Fig. 13 Velocity, angle of attack and angle of sideslip tracking, flight test.

Both filters result in very similar reconstructions for the rigid body signals and can follow the measured data closely. Across all flight test sections an average rms error of 1.4 deg for the aerodynamics angles and 2.6 deg for attitude angles was observed when compared to the FPR estimates. Therefore, even with all the additions to the filter, the rigid body signal reconstruction remains close to the traditional FPR results.

Another way to check the consistency of the filter is by looking at the estimated biases. In Fig. 14 the constant offset biases for the angle of attack and sideslip are presented for different flight test segments across all test flights. As can be seen, an average offset of around -5 deg and 2 deg is found for angle of attack and angle of sideslip respectively. Some outliers were also found with larger angle biases for more challenging flight test sections.

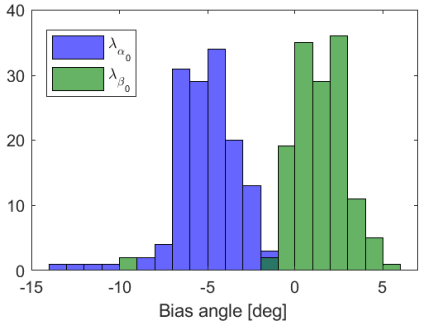

Fig. 14 Distribution of estimated aerodynamic angle biases across different flight test segments.

Next, the modal amplitude and velocity estimation using flight test data is evaluated. Again the filter estimate sensitivity to the number of included modes was assessed. In Fig. 15 and Fig. 16 the estimates for mode 1 and 3 are shown.

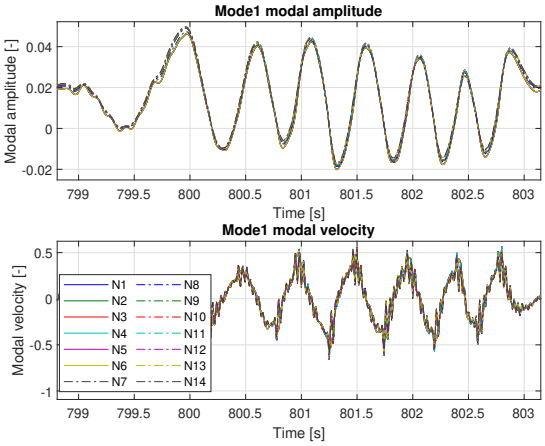

Fig. 15 Mode 1 amplitude and velocity tracking for varying number of modes in the filter.

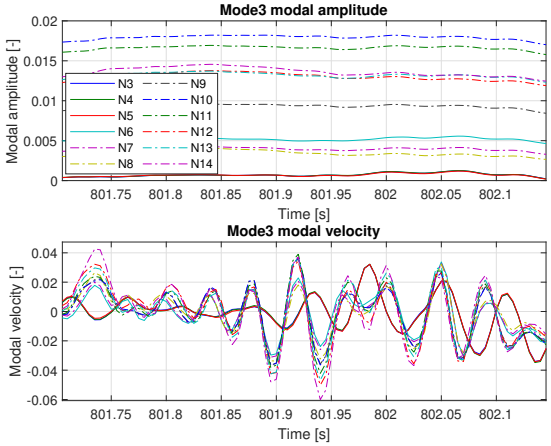

Fig. 16 Mode 3 amplitude and velocity tracking for varying number of modes in the filter.

For mode 1, it can be seen that the addition of extra modes in the filter does not have a significant effect on the modal estimates. However, for mode 3 there is a clear grouping in the velocity estimates that changes once mode 6 is added to the filter. Both mode 3 and 6 are related to the aircraft tail motion. Therefore, once mode 6 is added, there are enough degrees of freedom to separate the measured response into two different modes which changes the estimate. Similar to the results observed in the simulation study, different constant offsets are obtained for mode 3 amplitudes when modes are added and a better fit of the deformation is achieved.

Finally, the effect modes to the overall fit of sensor outputs was assessed. In Fig. 17, the average root mean squared error is determined across all the strain gauge and rotational rate measurements. It can be seen that after mode 8, additional modes do not lead to improvements in strain error as they become limited by the strain gauge noise level. Furthermore, some modes lead to larger improvements in strain fitting while others improve rotational rate fitting instead. Eventually, the error for both strain and rotational rate starts to increase again as the amount of modes starts to become too much for the given set of sensors.

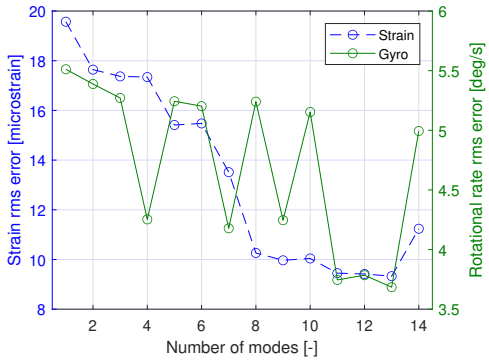

Fig. 17 Average strain and rotational rate measurement error for varying number of modes.

VI. Conclusion

In this paper, an extension to the flight path reconstruction filter was developed that is also able to reconstruct the aircraft modal amplitude and velocity signals. This is achieved by making use of additional measurements collected using accelerometers, gyroscopes and strain gauges placed across the aircraft structure. The developed filter is based on flexible aircraft kinematic equations and does therefore not require a flight dynamics model and is applicable to any aircraft. However, it is necessary to provide the displacement, rotation and strain mode shapes for the modes that wish to be reconstructed.

A scaled Diana 2 glider was used as a reference aircraft for this study. The performance of the filter was first evaluated using simulated responses from an aeroelastic flight dynamics model. In this case, both the aircraft rigid body states and the modal amplitude and velocity were accurately reconstructed from the noisy measurements. Furthermore, they showed to be insensitive to the number of modes used for the filter and inaccuracies in their shapes. As a final step, the filter was applied on flight test measurements where the rigid body estimates showed good agreement when compared to a traditional flight path reconstruction filter outputs. Secondly, the constant biases estimates for sensors were consistent across all flight tests. Finally, the modal amplitude and velocity estimation was also consistent for different number of modes included in the filter. Moreover, the addition of modes improved the fitting of rotational rate and strain responses.

Acknowledgments

The authors would like to thank the Netherlands Aerospace Centre Flight Physics and Loads department (AVFP) for the support and funding of this research project.

References

[1] Mulder, J. A., Chu, Q. P., Sridhar, J. K., Breeman, J. H., and Laban, M., "Non-linear aircraft flight path reconstruction review and new advances," *Progress in Aerospace Sciences*, Vol. 35, No. 7, 1999, pp. 673–726. https://doi.org/10.1016/s0376-0421(99)00005-6.

[2] Teixeira, B. O. S., Tôrres, L. A. B., Iscold, P., and Aguirre, L. A., "Flight path reconstruction – A comparison of nonlinear Kalman filter and smoother algorithms," *Aerospace Science and Technology*, Vol. 15, No. 1, 2011, pp. 60–71. https://doi.org/10.1016/j.ast.2010.07.005.

[3] Suh, P., "Robust Modal Filtering For Control Of Flexible Aircraft," Ph.D. thesis, Georgia Institute of Technology, 2014.

[4] Gherlone, M., Cerracchio, P., and Mattone, M., "Shape sensing methods: Review and experimental comparison on a wing-shaped plate," *Progress in Aerospace Sciences*, Vol. 99, 2018, p. 14–26. https://doi.org/10.1016/j.paerosci.2018.04.001.

[5] Derkevorkian, A., Masri, S. F., Alvarenga, J., Boussalis, H., Bakalyar, J., and Richards, W. L., "Strain-based deformation shape-estimation algorithm for control and monitoring applications," *AIAA Journal*, Vol. 51, No. 9, 2013, p. 2231–2240. https://doi.org/10.2514/1.j052215.

[6] Ma, Z., and Chen, X., "Fiber Bragg gratings sensors for Aircraft Wing Shape Measurement: Recent applications and technical analysis," *Sensors*, Vol. 19, No. 1, 2018, p. 55. https://doi.org/10.3390/s19010055.

[7] Barrows, D. A., and Liu, T., "Videogrammetric Model Deformation Measurement Technique for Wind Tunnel Applications," *Journal of Aircraft*, Vol. 38, 2001, pp. 745–754.

[8] Burner, A. W., Lokos, W. A., and Barrows, D. A., *Aeroelastic Deformation: Adaptation of Wind Tunnel Measurement Concepts to Full-Scale Vehicle Flight Testing*, TM-2005-213790, NASA Langley Research Center, 2005.

[9] Mkhoyan, T., de Visser, C., and Breuker, R. D., "Adaptive real-time clustering method for dynamic visual tracking of very flexible wings," American Institute of Aeronautics and Astronautics Inc, AIAA, 2020. https://doi.org/10.2514/6.2020-2250.

[10] Kotikalpudi, A., Schmidt, D. K., Regan, C. D., and Seiler, P. J., "Real-time shape estimation for flexible unmanned air vehicle via Kalman filtering," *AIAA Scitech 2020 Forum*, 2020. https://doi.org/10.2514/6.2020-1267.

[11] Lustosa, L. R., Kolmanovsky, I., Cesnik, C. E., and Vetrano, F., "Aided inertial estimation of wing shape," *Journal of Guidance, Control, and Dynamics*, Vol. 44, No. 2, 2021, p. 210–219. https://doi.org/10.2514/1.g005368.

[12] Schirmer, G., Steck, J. E., and Chakravarthy, A., "Design, implementation and experimental testing of an inertial sensor system to quantify wing deflection," *AIAA Scitech 2019 Forum*, 2019. https://doi.org/10.2514/6.2019-1539.

[13] Waszak, M. R., and Schmidt, D. K., "Flight dynamics of aeroelastic vehicles," *Journal of Aircraft*, Vol. 25, No. 6, 1988, pp. 563–571. https://doi.org/10.2514/3.45623.

[14] Grauer, J. A., and Boucher, M. J., *Output Measurement Equations for Flexible Aircraft Flight Dynamics*, TM–2018–220102, NASA Langley Research Center, 2018.

[15] Jurisson, A., de Breuker, R., de Visser, C., Eussen, B., and Timmermans, H., "Aeroservoelastic flight testing platform development for system identification," AIAA SciTech, AIAA, 2022, p. 13. https://doi.org/10.2514/6.2022-2169.

[16] Jurisson, A., Timmermans, H., Eussen, B., de Visser, C., and de Breuker, R., "Ground vibration testing and FEM model updating of scaled Diana 2 glider model using accelerometer, gyro and strain measurements," International Forum on Aeroelasticity and Structural Dynamics, IFASD, 2022, p. 10.